Nano Research

Open Access

Research Article

Local electric field engineering via ferroelectric substrates for enhanced oxygen reduction reaction on single-atom catalysts

Yangfan Shao[§], Zhichao Zhang[§], and Jia Li ✉

Shenzhen Geim Graphene Center and Institute of Materials Research, Tsinghua Shenzhen International Graduate School, Tsinghua University, Shenzhen 518055, China

[§] *Yangfan Shao and Zhichao Zhang contributed equally to this work.*

Cite this article: *Nano Research*, **2026**, *19*, 94908460. https://doi.org/10.26599/NR.2026.94908460

ABSTRACT: Environmental factors at electrochemical interfaces, such as the local electric field, are widely recognized as critical determinants of catalytic performance, which could strongly influence reaction pathways and kinetics. However, strategies that leverage these effects to precisely control catalytic activity are limited. In this study, using grand canonical potential density functional theory, we demonstrate that combining single-atom catalysts (SACs) with ferroelectric substrates is a powerful solution. The modified local electric field significantly weakens the adsorption of the *OH intermediate in the oxygen reduction reaction (ORR) on the FeN_4–C catalyst. By establishing a physical model, we reveal that the local electric field is primarily modified by surface charges induced by the applied potential and the intrinsic dipole moment of the substrate. Our findings highlight the significant role of local electric fields in tailoring catalytic mechanism, and pave the way for a promising substate engineering approach in the rational design of high-performance electrocatalytic devices.

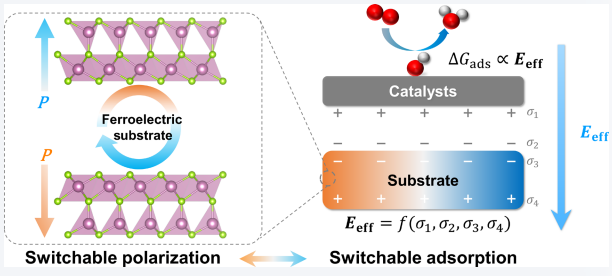

KEYWORDS: local electric field, oxygen reduction reaction, substrate engineering, grand canonical density functional theory (DFT), single atom catalyst

1 Introduction

The oxygen reduction reaction (ORR) is the key cathodic process in most fuel cells, enabling the conversion of chemical energy from sustainable fuels, such as hydrogen and alcohols, into electricity under mild electrochemical conditions [1]. However, the sluggish kinetics and thermodynamics of the ORR largely hinder the overall efficiency of fuel cell systems, particularly in proton exchange membrane fuel cells (PEMFCs) [2], where the reaction rate is much slower than that of the anodic hydrogen oxidation reaction (HOR) [3]. Currently, platinum-based catalysts, such as the commercially available Pt/C, remain the benchmark for ORR electrocatalysis [4, 5]. Nevertheless, the high cost and limited availability of Pt severely impede its widespread use. Therefore, developing high-performance, earth-abundant ORR catalysts is essential for advancing fuel cell technologies and expanding their role in sustainable energy conversion [6–9].

Received: November 28, 2025; **Revised:** December 30, 2025
Accepted: January 16, 2026

✉Address correspondence to li.jia@sz.tsinghua.edu.cn

Recently, single-atom catalysts (SACs) have emerged as a promising alternative to conventional noble-metal catalysts. Due to the maximized utilization of active sites, SACs featuring atomically dispersed metal centers achieve significantly enhanced mass activity [10–13]. Among the diverse SAC systems, metal–nitrogen co-doped carbon materials (M–N–C) are especially attractive because their catalytic performance can be flexibly tuned through the well-defined planar coordination environment of active centers [14]. This tunability benefits from the unique properties of carbon-based systems, including graphene and phthalocyanine- or phosphide-derived molecular structures. Building on these advantages, iron-based FeN_4–C catalysts have been demonstrated to have outstanding ORR activity, approaching that of commercial Pt/C catalysts [15–17]. However, according to Sabatier's principle, optimal activity requires an intermediate binding strength that is not too weak or too strong [18]. Similar to Pt, the adsorption strength of *OH on FeN_4 sites also deviates from the optimal, demanding further fine-tuning of the activity [19].

Traditionally, efforts to fine-tune catalytic activity have primarily focused on engineering the catalyst itself, through approaches, such as heteroatom doping, defect engineering, curvature modulation, and axial coordination [4, 18–23]. However, in practice, environmental factors, including electrolyte composition, applied

potential, and substrate properties, can also significantly influence catalytic mechanisms and performance [24–27]. For instance, the adsorption strengths of polar intermediates, such as *CO_2, have been shown to strongly correlate with the direction and magnitude of local electric fields [28]. Nevertheless, directly applying an external electric field ($\boldsymbol{E}_{elec}$) within the electric double layer remains challenging. To overcome this limitation, researchers have developed catalysts with needle-like morphologies to exploit the tip effect, which enhances local charge density and strengthens the electric field between the catalyst surface and counterions [29, 30]. Since most nanocatalysts require substrates for practical fabrication and operation, substrate engineering is another effective strategy for improving catalytic performance. A proper substrate can reorganize the local microenvironment, regulate the spillover of reactants and intermediates, and even directly modify the electronic structure of active sites [31–34]. In the context of electric field effects, ferroelectric materials, which are characterized by spontaneous polarization, can induce intrinsic electric fields that may alter the local electronic environment in a manner similar to an applied bias [35]. Moreover, polarization switching reverses surface band alignment, resulting in different interfacial contact and charge-transfer characteristics. This dynamic modulation creates variable and practical electric fields at the catalyst–substrate interface, thereby opening new opportunities for tuning catalytic reactions *in situ* [36–38].

In this work, employing a constant-potential electrocatalytic simulation framework, we investigated the influence of local electric fields on ORR performance at a model system of FeN_4–C supported on In_2Se_3. We demonstrate that introducing a ferroelectric substrate provides an effective strategy for modulating both the local electric field and the adsorption strength of reaction intermediates, with *OH adsorption notably weakened on FeN_4–C@In_2Se_3. After evaluating the contributions of individual charged components, we developed a physical model to elucidate the underlying mechanism, and determined that the local electric field around intermediates is primarily governed by the combined effects of surface charging induced by the applied potential and the intrinsic dipole ($\boldsymbol{\mu}$) of ferroelectric substrate. These findings highlight the potential of substrate engineering as a powerful approach to utilize environmental factors in designing high-performance electrocatalysts.

2 Results and discussion

The interaction between a catalyst and its supporting substrate can significantly affect the electronic structure of the catalyst, as illustrated schematically by the band alignment diagrams in Fig. 1(a). When the Fermi level of a SAC lies below the valence band maximum (VBM) of the substrate, charge transfers from the substrate to the SAC. This process negatively charges the catalyst and induces an interfacial dipole pointing from the catalyst to the substrate, accompanied by a local electric field. Conversely, if the Fermi level of the SAC is above the conduction band minimum (CBM) of the substrate, the direction of charge transfer is reversed, resulting in an oppositely oriented dipole and electric field. When a ferroelectric material is used as the substrate, its effect on the interfacial electronic properties is more complicated and can be divided into two aspects. First, the intrinsic spontaneous polarization of the ferroelectric material couples with the dipole generated by charge transfer, further modifying the local electric field near the interface. Second, the switchable polarization direction of ferroelectrics shifts the band alignment (Figs. 1(a)

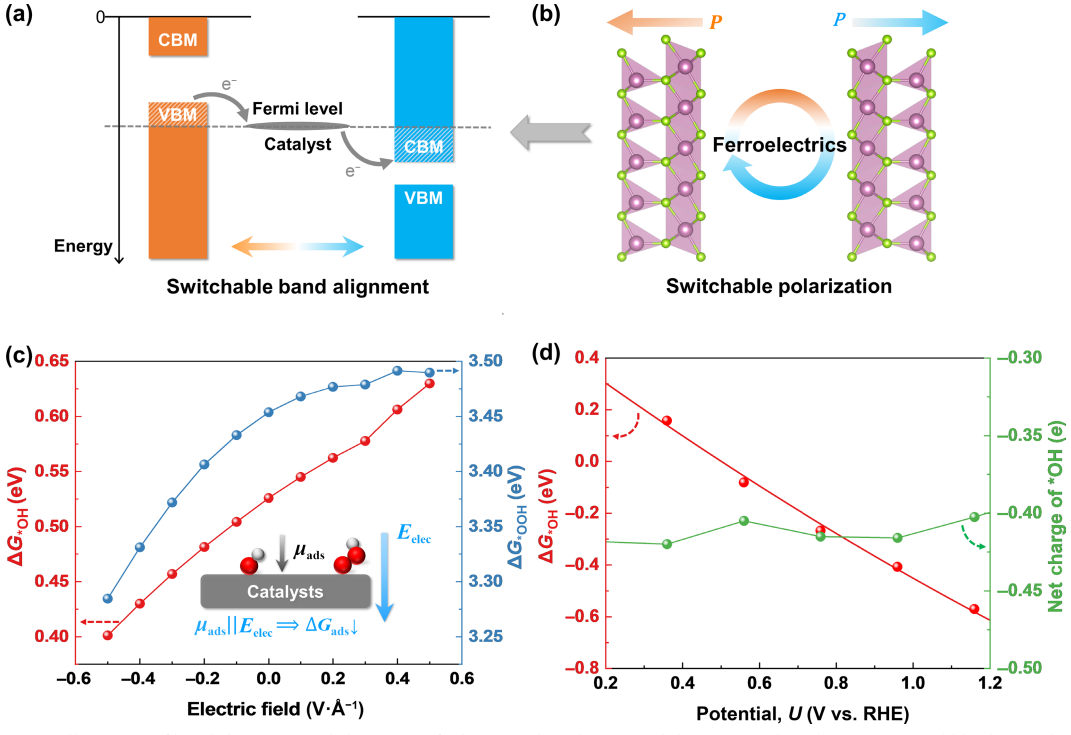

Figure 1 (a) Schematic illustration of band alignment and charge transfer between the substrate and the supported catalyst. Orange and blue bars indicate different band structures of substrates, highlighting the positions of CBM and VBM, while grey dashed line indicates the Fermi level of the supported catalyst. (b) Schematic of switchable dipole orientations in a ferroelectric system, exemplified by A_2B_3-type materials. (c) Effect of an applied electric field on the adsorption of *OH and *OOH intermediates on FeN_4–C. Insets depict the corresponding adsorption configurations, where red and white spheres represent O and H atoms. (d) Adsorption energy and net charge of the *OH intermediates on FeN_4–C as a function of electrode potential.

and 1(b)), affecting charge transfer behavior simultaneously. These two effects combine to modulate the adsorption strength of catalytic intermediates, although the detailed mechanisms and design principles underlying this modulation remain insufficiently investigated.

As a proof of concept, we examined ORR on FeN_4–C as a model system. Similar to Pt (111), thermodynamic results show that FeN_4–C binds the *OH intermediate slightly too strongly, making the desorption of *OH to form OH^-/H_2O as the potential-limiting step (Fig. S1 in the Electronic Supplementary Material (ESM)). Therefore, weakening the *OH adsorption is expected to enhance ORR activity. To further explore the influence of the electric field on the adsorption behavior of reaction intermediates, we applied a series of external electric fields along the *z*-axis and investigated the interaction between the field and the intermediates, with the results shown in Fig. 1(c) and Fig. S2 in the ESM. Generally, a positive electric field along the *z*-axis weakens the adsorption of *OH and *OOH, while a negative field strengthens it. Notably, the two intermediates exhibit distinct response characteristics to field strength. The *OH adsorption energy varies almost linearly with the electric field, while the *OOH adsorption energy varies quadratically. These observations suggest that applying an external electric field could effectively break the conventional scaling relationship and modulate the adsorption energy difference (the Gibbs free energy difference between OOH and OH, $\Delta G_{*OOH} - \Delta G_{*OH}$), to optimize the catalytic activity of SACs.

This phenomenon can be explained by dipole-field interaction, as described by Eq. (1) [39, 40]

$$\Delta G_{\text{field}} = -\boldsymbol{\mu}\boldsymbol{E}_{\text{elec}} - \frac{1}{2}\alpha \boldsymbol{E}_{\text{elec}}^{\ 2} + \ldots \quad (1)$$

Here, ΔG_{field} represents the interaction energy between a $\boldsymbol{\mu}$ and an $\boldsymbol{E}_{\text{elec}}$. The term α denotes the polarizability of the intermediate and quantifies its ability to redistribute charge in response to the applied field. The first term of Eq. (1) accounts for the interaction between the intrinsic dipole moment of the intermediate and the electric field. Stabilization occurs when $\boldsymbol{\mu}$ is aligned parallel to $\boldsymbol{E}_{\text{elec}}$, while antiparallel alignment leads to destabilization. The second term represents the field-induced dipole effect, which always contributes a stabilizing interaction.

In our system, electron transfer from the FeN_4–C catalyst to the *O, *OH, or *OOH intermediate generates a downward-oriented negative dipole along the *z*-axis ($-\vec{z}$, Fig. S3 in the ESM). Consequently, an external electric field pointing along the $-\vec{z}$ direction strengthens the adsorption of the *O, *OH, and *OOH intermediates, whereas a field along the $+\vec{z}$ direction weakens it. These intermediates exhibit distinct response behaviors due to their different polarizabilities. By applying quadratic fitting to Fig. 1(c) and Fig. S2 in the ESM, the quadratic term in Eq. (1) can be neglected for *O and *OH, as their polarizabilities are relatively small (0.05 and 0.08 e·Å^2·V^{-1}, respectively). In contrast, the *OOH intermediate has a much larger polarizability of 0.52 e·Å^2·V^{-1}, which makes the quadratic term dominant in its field response. Consequently, *OOH shows a pronounced nonlinear dependence of adsorption energy on the electric field. This behavior is consistent with increasing molecular complexity from *O to *OOH. With more atoms and bonds, *OOH exhibits more substantial interfacial charge redistribution and structural reorganization under an applied field, leading to nonlinear modulation of adsorption energetics. These results validate the fundamental principle of electric-field-mediated tuning of catalytic activity and suggest that, for the FeN_4–C catalyst, generating an electric field along the $+\vec{z}$ direction is an effective strategy to weaken *OH adsorption and improve ORR activity.

However, for a realistic system employing a ferroelectric substrate, generating a local electric field along the desired orientation is more complex. In electrochemical processes, both the catalysts and the substrates are substantially charged by the external applied potential, which can overlap with the adsorption- and band-alignment-induced charge transfer. As a first-order approximation, the quadratic term in Eq. (1) can be neglected for *OH due to its small polarizability. Grand canonical calculations further demonstrate that, under various applied potentials and surface charge states, *OH consistently carries a net charge of approximately −0.4e (Fig. 1(d)). This allows us to treat the adsorbate-based dipole as consisting of separate positive and negative centers. The *OH serves as a negative point charge (q_{ads} = −0.4e, the position of q_{ads} is defined as the atomic position of the oxygen atom in the adsorbed *OH), while the corresponding positive charge on FeN_4–C merges with the externally injected charges induced by the applied potential (Fig. 2).

Thus, Eq. (1) can be simplified into a point-charge-field interaction model as Eq. (2)

$$\Delta G_{\text{field}} = q_{\text{ads}}\phi \quad (2)$$

Here, ϕ denotes the electrostatic potential at the position of q_{ads}, arising from the effective electric field ($\boldsymbol{E}_{\text{eff}}$) generated by surface charges on FeN_4–C, substrate polarization and so on. For simplicity, the charged FeN_4–C and the substrate can be considered as two parallel layers with uniform charge densities (σ_1, σ_2). Likewise, the spontaneous polarization of the ferroelectric substrate can be represented by two oppositely charged layers (σ_3, σ_4, $\sigma_3 = \sigma_4$). At a position above all these layers, the total effective external electric field can be expressed as Eq. (3)

$$\boldsymbol{E}_{\text{eff}} = \sum_{k=1}^{4} \frac{\sigma_k}{2\varepsilon_0}\vec{z} \quad (3)$$

where σ_k is the surface charge density of the k^{th} layer and ε_0 is the vacuum permittivity. Ideally, the bound charges of the ferroelectric substrate and the interfacial charges at the FeN_4–C/substrate interface would fully compensate each other. In practice, however, deviations arise due to electrostatic screening, ferroelectric domain

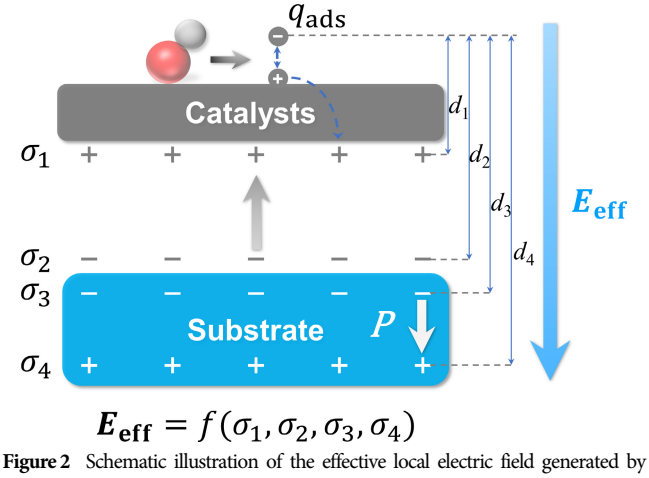

Figure 2 Schematic illustration of the effective local electric field generated by the ferroelectric substrate.

effects, and other nonidealities. To account for these factors, an effective screening coefficient (β_k) is introduced for each charged layer, leading to Eq. (4)

$$\boldsymbol{E}_{\text{eff}}{}' = \frac{1}{2\varepsilon_0}\sum_{k=1}^{4}\beta_k\sigma_k\vec{\boldsymbol{z}}, \quad 0 < \beta_k < 1 \tag{4}$$

Here, $\boldsymbol{E}_{\text{eff}}{}'$ represents the effective electric field strength that adsorbates experience, β_k quantifies the degree of electrostatic associated with each charged layer. It is reasonable to assume $\beta_1 > \beta_2 > \beta_3 > \beta_4$, since the electric field from deeper layers is increasingly screened by overlying materials before reaching the adsorbate. Since Eq. (4) represents a uniform electric field, the electrostatic potential at q_{ads} and the corresponding interaction energy can be expressed as Eq. (5)

$$\Delta G_{\text{field}} = q_{\text{ads}}\phi = \frac{q_{\text{ads}}}{2\varepsilon_0}\sum_{k=1}^{4}\beta_k\sigma_k d_k \tag{5}$$

where d_k denotes the distance between each charged layer and the adsorbate. From Eq. (5), one can see that ΔG_{field} is determined by the summation term $\sum_k\beta_k\sigma_k d_k$. Taking a free-standing FeN_4–C as an example ($\sigma_2 = \sigma_3 = \sigma_4 = 0$), the surface becomes positively charged under working potentials ($\sigma_1 > 0$). For an adsorbed *OH species with $q_{\text{ads}} = -0.4$e, decreasing the surface positive charge σ_1 increase ΔG_{field}, thereby destabilizing *OH adsorption. However, the contributions of the substrate layers ($\sigma_2 \sim \sigma_4$) require density functional theory (DFT) calculations for further insight.

In an initial attempt to identify suitable ferroelectric candidates, we evaluated the band alignment between FeN_4–C and nine ferroelectric materials from the A_2B_3 (A = Al, Ga, and In; B = S, Se, and Te) family under two opposite polarization orientations. As shown in Fig. 3(a), in most cases, the Fermi level of FeN_4–C lies above the CBM of the ferroelectric materials. As a proof of concept, we used FeN_4–C on an In_2Se_3 substrate as a model system. At the potential of zero charge (PZC), two opposite polarization orientations of In_2Se_3 are considered and denoted as $In_2Se_3\uparrow$ (In_2Se_3 with upward polarization) and In_2Se_3 with downward polarization ($In_2Se_3\downarrow$), respectively (Figs. 3(b) and 3(c)). Various stacking configurations were examined to construct the FeN_4–C/In_2Se_3 heterostructure, and the most stable heterostructure occurs when the Fe atom of FeN_4–C is located directly above a Se atom in the substrate for both polarization states (Fig. S4 in the ESM). As shown in Fig. 3(a), the Fermi level of FeN_4–C (−3.94 eV) lies above the CBM of In_2Se_3 for both polarization orientations, with the E_{CBM} (E_{CBM} denotes the CBM energy level) at −4.44 and −5.62 eV for $In_2Se_3\uparrow$ and $In_2Se_3\downarrow$, respectively. This facilitates electron transfer from FeN_4–C to the substrate in the same direction but with different magnitudes. Bader charge analysis confirms that FeN_4–C loses 0.017e when interfaced with $In_2Se_3\uparrow$ and 0.290 e with $In_2Se_3\downarrow$ (Figs. 3(b) and 3(c)), corresponding to surface charge densities (σ_2) of 0.00013 and −0.0022 e·Å^{-2}, respectively. Electronic structures shown in Fig. 3(d) indicate that the VBM of In_2Se_3 shifts downward in the FeN_4–C@$In_2Se_3\downarrow$ system, consistently indicating increased electron injection into the conduction band of In_2Se_3. The interfacial charge distribution and spin-polarization coupling caused by ferroelectric polarization also lead to magnetic changes. The calculated magnetic moment of the Fe center decreases from 1.915 Bohr magneton (μ_B) in free-standing FeN_4–C to 1.863 μ_B in the FeN_4–C@$In_2Se_3\uparrow$ system and drops further to 0.682 μ_B in the FeN_4–C@$In_2Se_3\downarrow$ system. Different polarization directions modify the local electronic environment surrounding the Fe site, thereby tuning its spin state and the corresponding magnetic moment. Our grand-canonical DFT framework naturally accounts for these magnetic variations, which act synergistically with electric-field and charge-transfer effects to regulate ORR activity.

However, this electron transfer charges the FeN_4–C more positively. According to Eq. (5), an increased value of $\beta_1\sigma_1 d_1 + \beta_2\sigma_2 d_2$ appears unfavorable for weakening *OH adsorption. However, it is noted that the contribution from the intrinsic polarization of the substrate, i.e., σ_3 and σ_4, has not yet been included. DFT calculations indicate that the intrinsic dipole moment of In_2Se_3 is about ±0.09 e·Å per unit cell (Fig. S5 in the ESM), along with a charge-center separation of $d_3 - d_4 = 0.17$ Å (the distance between the average z-positions of two In layers and three Se layers). Therefore, the corresponding σ_3 and σ_4 are estimated to be ±0.036 e·Å^{-2}, which is one order of magnitude greater than the band-alignment induced charge transfer of −0.0022 e·Å^{-2}. Although opposite charges, σ_3 and σ_4, partially cancel each other out, their net influence cannot be neglected. Further grand canonical simulations are necessary to incorporate all these effects simultaneously.

Accordingly, a series of applied potentials and the corresponding surface charge states were modeled for three systems, FeN_4–C, FeN_4–C@$In_2Se_3\uparrow$, and FeN_4–C@$In_2Se_3\downarrow$. The ORR activity of each system was evaluated across a broad pH range, from acidic (pH = 1) to alkaline (pH = 13), to capture the electrochemical conditions. Figure 4 shows the free energy profiles of each elementary ORR step. Compared to the free-standing FeN_4–C, both the FeN_4–C@$In_2Se_3\uparrow$ and FeN_4–C@$In_2Se_3\downarrow$ systems exhibit higher ORR limiting potential under all considered pH conditions. Notably, the FeN_4–C@$In_2Se_3\downarrow$ system shows the best performance in acid conditions, with a low overpotential of 0.35 V. This enhancement primarily arises from the modified energetics of the final reaction step, *OH protonation to H_2O. As shown in Figs. 4(a)–4(c), the reaction free energy of this step decreases progressively, thereby reducing the overall ORR overpotential. In Fig. 4(c), the *OH protonation step becomes more favorable than the *O protonation step, making it the new potential determining step. The same trend is also preserved under alkaline conditions.

These results confirmed our earlier assumption that the unfavorable band alignment alone cannot fully determine the overall influence of the substrate on *OH adsorption strength. The underlying mechanism can then be analyzed within the framework of Eq. (5). Taking an applied potential of 0.56 V vs. reversible hydrogen electrode (V_{RHE}) as an example, Tables 1 and 2 summarize the charge distributions (σ_k and q_{ads}) and relative distance features (d_k) of *OH-adsorbed systems in acidic conditions.

Substituting the data from Tables 1 and 2 into Eq. (5)

$$\Delta G_{\text{field}}\,(\text{eV}) = \frac{q_{\text{ads}}}{2\varepsilon_0}\sum_{k=1}^{4}\beta_k\sigma_k d_k = \begin{cases} -0.81\beta_1, \text{FeN}_4-\text{C} \\ -0.41\beta_1 + 0.14\beta_2 - 11.81\beta_3 + 12.07\beta_4, \text{FeN}_4-\text{C@In}_2\text{Se}_3\uparrow \\ -0.59\beta_1 - 0.29\beta_2 + 11.64\beta_3 - 11.82\beta_4, \text{FeN}_4-\text{C@In}_2\text{Se}_3\downarrow \end{cases} \tag{6}$$

Note that a dimensional conversion to express energy in eV was performed. It is noted that $1 > \beta_1 > \beta_2 > \beta_3 > \beta_4 > 0$. The first and second terms (β_1, β_2-related) represent the contribution of surface charges, denoted as $\Delta G_{\text{surface}}$, which is mainly induced by the external

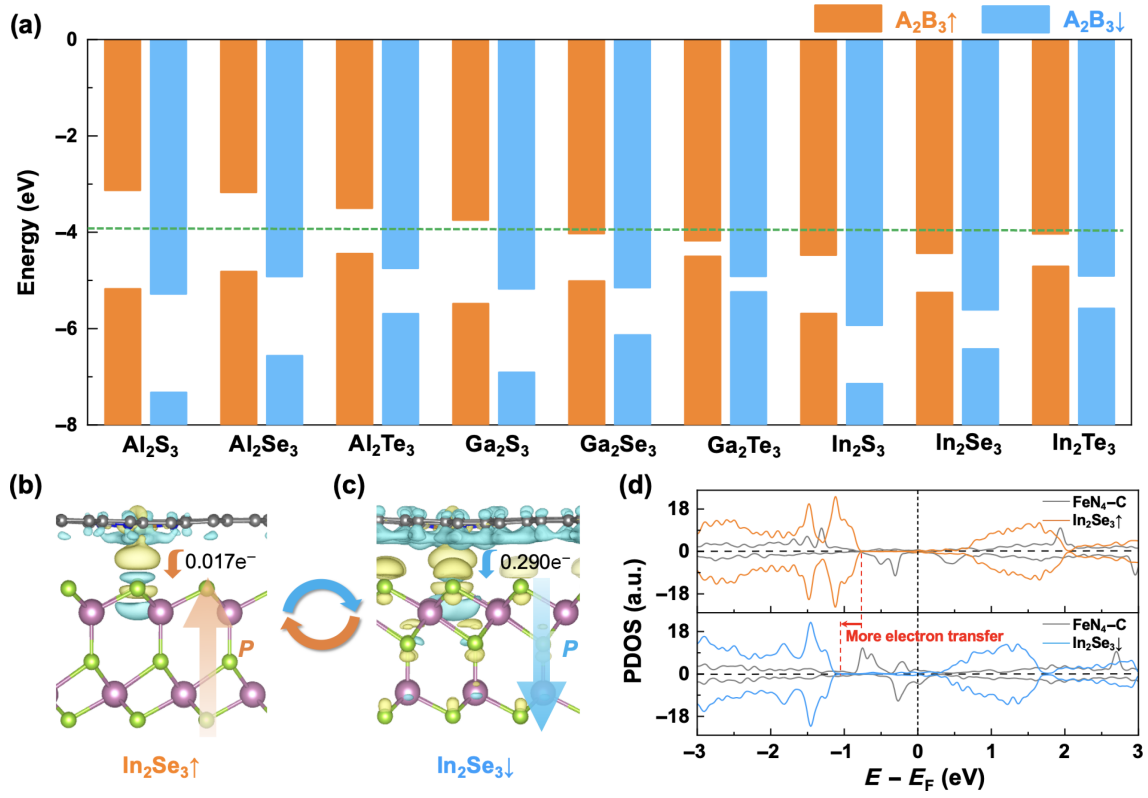

Figure 3 (a) Band alignment between FeN_4–C and A_2B_3-type ferroelectrics (A = Al, Ga, and In; B = S, Se, and Te). The green line represents the position of the Fermi level of FeN_4–C. Charge density difference at the FeN_4–C/In_2Se_3 interface for (b) In_2Se_3↑ and (c) In_2Se_3↓. Grey, purple, and green spheres represent C, In, and Se atoms. Yellow and light-blue isosurfaces indicate charge accumulation and depletion, with an isovalue of 0.0005 e·Bohr^{-3}. (d) Partial density of states (PDOS) for FeN_4–C supported on In_2Se_3↑ and In_2Se_3↓ substrates.

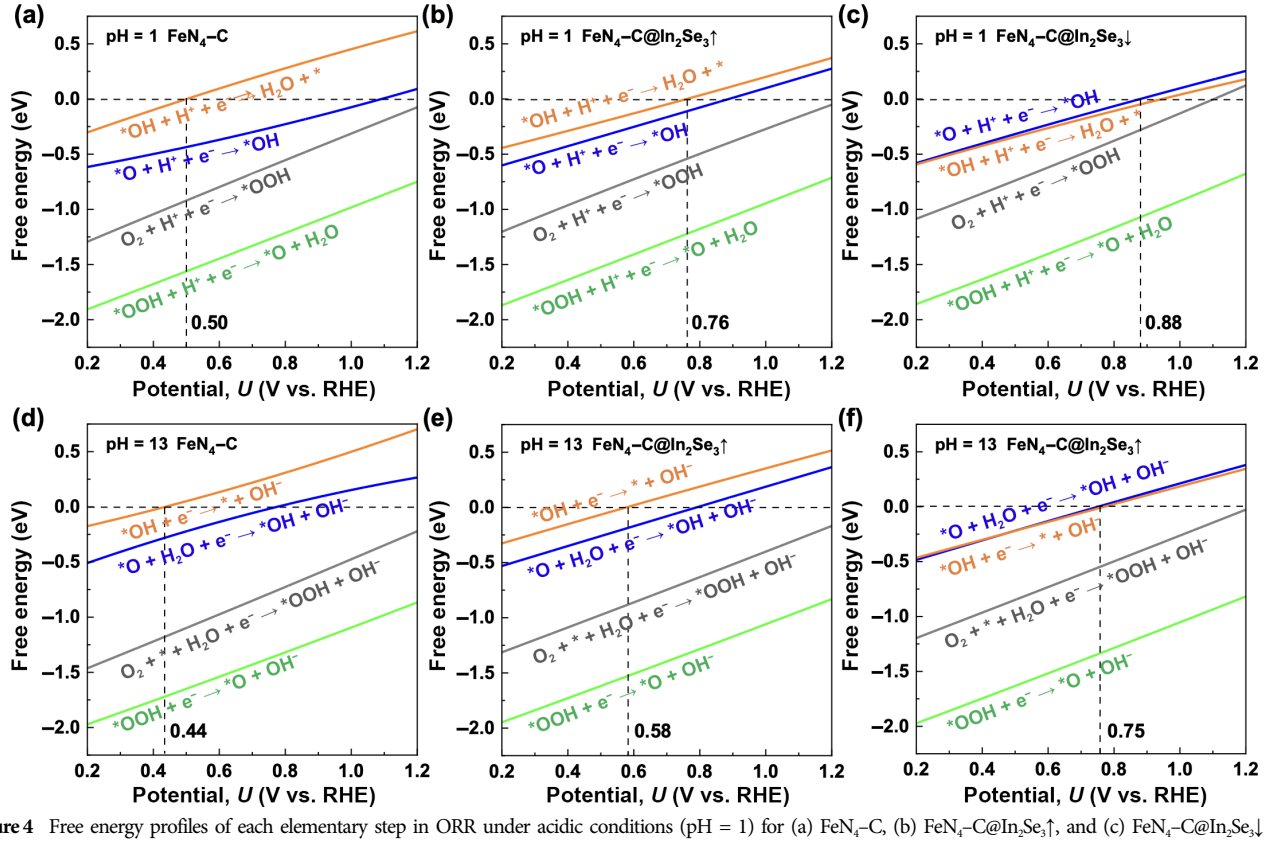

Figure 4 Free energy profiles of each elementary step in ORR under acidic conditions (pH = 1) for (a) FeN_4–C, (b) FeN_4–C@In_2Se_3↑, and (c) FeN_4–C@In_2Se_3↓ as a function of electrode potential. Corresponding free energy profiles under alkaline conditions (pH = 13) are shown for (d) FeN_4–C, (e) FeN_4–C@In_2Se_3↑, and (f) FeN_4–C@In_2Se_3↓.

Table 1 Charge distribution of *OH adsorbed FeN_4–C, FeN_4–C@In_2Se_3↑, and FeN_4–C@In_2Se_3↓ systems

System	Total net charge (e·Å^{-2})	σ_1 (e·Å^{-2})[a]	σ_2 (e·Å^{-2})[a]	σ_3 (e·Å^{-2})[a]	σ_4 (e·Å^{-2})[a]	q_{ads} (e)
FeN_4–C	1.16	1.20×10^{-2}	—	—	—	−0.41
FeN_4–C@In_2Se_3↑	0.30	6.02×10^{-2}	-6.86×10^{-4}	3.63×10^{-2}	-3.63×10^{-2}	−0.41
FeN_4–C@In_2Se_3↓	0.96	8.76×10^{-3}	1.45×10^{-3}	-3.63×10^{-2}	3.63×10^{-2}	−0.38

[a]Definition of σ_k (k = 1–4) are illustrated in Fig. 2.

Table 2 Distance-related structural parameters of *OH adsorbed FeN_4–C, FeN_4–C@In_2Se_3↑, and FeN_4–C@In_2Se_3↓ systems

System	d_1 (Å)[a]	d_2 (Å)[a]	d_3 (Å)[a]	d_4 (Å)[a]
FeN_4–C	1.82	—	—	—
FeN_4–C@In_2Se_3↑	1.82	5.48	8.78	8.97
FeN_4–C@In_2Se_3↓	1.82	5.41	8.65	8.79

[a]Definition of d_k (k = 1–4) are illustrated in Fig. 2.

applied potential and interfacial charge transfer induced by band alignment. The third and fourth terms (β_3, β_4-related) represent the role of the intrinsic dipole of the In_2Se_3 substrate, i.e., the bound charges, denoted as ΔG_{bound}. Although the absolute value of each bound charge term is much higher than the surface charge term, the final contributions could be comparable after the cancellation of opposite bound charges, as will be shown below.

First, we consider the contribution of the surface charge, $\Delta G_{surface}$. Since the surface charge on FeN_4–C (σ_1) interacts directly with *OH, σ_1 dominates the surface charge part. Both substrate-mediated systems carry less net positive surface charge (Table 1), resulting in higher $\Delta G_{surface}$ values and thus destabilized *OH adsorption. This explains why *OH binds less strongly in the substrate-mediated systems. However, the $\Delta G_{surface}$ term alone cannot explain the relative adsorption strengths between FeN_4–C@In_2Se_3↑ and FeN_4–C@In_2Se_3↓. DFT results show that *OH binds more weakly to FeN_4–C@In_2Se_3↓, yet charge distribution analysis reveals a larger positive charge in this system. This discrepancy can be resolved by considering the intrinsic dipole contribution from In_2Se_3, i.e., ΔG_{bound}. FeN_4–C@In_2Se_3↑ and FeN_4–C@In_2Se_3↓ systems in Eq. (6) show that the sign of ΔG_{bound} is opposite in these two systems: negative in FeN_4–C@In_2Se_3↑ system in Eq. (6) and positive in FeN_4–C@In_2Se_3↓ system in Eq. (6). This increases the total ΔG value for the FeN_4–C@In_2Se_3↑ system, further weakening *OH adsorption, while strengthening its adsorption on FeN_4–C@In_2Se_3↓. This additional contribution ultimately reverses their relative magnitudes.

In addition, since *OH adsorption energies can be obtained directly from DFT calculations, we can quantitively analyze the relative contributions of these two parts further. Note that the adsorption energy cannot be directly considered equal to ΔG_{field} in Eq. (5), because Eq. (5) only represents the electrostatic contribution, which depends on the definition of absolute zero point. However, the relative energy differences properly reflect variations in ΔG_{field} in various systems. Extracting the *OH adsorption energies in three systems at 0.56 V_{RHE} from Fig. 4 yields Eqs. (7) and (8)

$$\Delta G_{field}(FeN_4C@In_2Se_3\uparrow) - \Delta G(FeN_4C) = 0.209\ eV \quad (7)$$

$$\Delta G_{field}(FeN_4C@In_2Se_3\downarrow) - \Delta G(FeN_4C) = 0.344\ eV \quad (8)$$

Since the surface charge on FeN_4–C (σ_1) interacts directly with *OH, we can reasonably assume that β_1 = 1. Substituting Eq. (6) into Eqs. (7) and (8) and using β_3 as a common parameter yields the following results

$$\beta_1 = 1 \quad (9)$$

$$\beta_2 = 0.49\beta_3 + 0.41 \quad (10)$$

$$\beta_4 = 0.97\beta_3 - 0.02 \quad (11)$$

where β_2 mainly originates from the screening effect of FeN_4–C, while β_3 and β_4 further involve the screening effect of In_2Se_3. Further determining the absolute value of each coefficient is difficult. Therefore, in the following, we will take β_2 = 0.5 as an example. Considering the metallic feature of the graphene layer, 0.5 is a relatively conservative estimate. Then, β_1, β_2, β_3, and β_4 can be obtained as approximately 1, 0.5, 0.18, and 0.15, respectively, and thus Eq. (6) becomes

$$\Delta G_{field}(eV) = \begin{cases} -0.81, FeN_4\text{–}C \\ -0.34 - 0.32 = -0.66, FeN_4\text{–}C@In_2Se_3\uparrow \\ -0.74 + 0.32 = -0.41, FeN_4\text{–}C@In_2Se_3\downarrow \end{cases} \quad (12)$$

Here, −0.81, −0.34 and −0.74 represent the contribution of $\Delta G_{surface}$, while −0.32 and 0.32 represent that of ΔG_{bound}. In general, the introduction of an In_2Se_3 substrate significantly reduces the stabilizing effect of the net surface positive charges on *OH adsorption, regardless of its polarization orientation. This weakens *OH adsorption on both substrate-mediated systems. However, when comparing these two systems, the ΔG_{bound} term dominates. After canceling out the opposite bound charges, the magnitude of ΔG_{bound} is still comparable to that of $\Delta G_{surface}$. The opposite sign of ΔG_{bound} with various polarization orientations of In_2Se_3 ultimately reverses the relative magnitude of total ΔG.

In addition, in many catalytic systems, the d-band center of transition metal sites is strongly correlated with the adsorption strength of intermediates and overall catalytic activity [41, 42]. However, substrate-induced interfacial effects can partially obscure the predictive capability of the conventional d-band center theory. A detailed electronic structure analysis of FeN_4–C, FeN_4–C@In_2Se_3↑, and FeN_4–C@In_2Se_3↓ were conducted, whose d-

band centers were calculated to be −1.31, −1.11, and −0.55 eV, respectively. Generally, an upward shift of the d-band center indicates stronger interactions between Fe the 3d states and oxygen-containing intermediates. However, despite this trend, DFT results show that the adsorption of a key intermediate, such as *OH, is significantly weaker on the ferroelectric substrate. This apparent discrepancy can be explained by considering the combined effects of interfacial charge redistribution and field-induced electrostatic interactions. There effects collectively regulate the adsorption behavior, which cannot be fully captured by a single d-band center descriptor. These could also provide insight into future theoretical catalytic analyses.

These results demonstrate the consistency between catalytic performance and local electric field strength, and validates the reliability of our proposed model. Furthermore, our findings highlight the potential to utilize the local electric field to modulate the kinetics of electrochemical reactions in practice. While directly applying or modifying electric fields within the electric double layer is challenging, ferroelectric materials provide a straightforward and tunable platform for achieving this effect. Appropriately selected ferroelectric substrates can significantly influence catalytic reactions. However, simple screening based solely on band alignment is insufficient because surface charging, induced by the applied potential and the intrinsic dipole of ferroelectrics, can substantially alter initial predictions. Therefore, additional simulations under realistic working potentials using explicit catalyst–substrate heterostructure models are essential. We believe the model proposed in this work provides valuable insights for designing next-generation electrocatalytic devices.

3 Conclusions

In summary, we propose a strategy to enhance ORR activity of SACs by coupling them with ferroelectric substrates to synergistically modulate the strength and direction of local electric fields. The externally applied potential induces substantial surface charging, and the ferroelectric polarization of the substrate allows for the fine-tuning of the interfacial electric field. As proof of concept, we demonstrated this strategy using a FeN_4–C catalyst supported on In_2Se_3. After involving the constant potential condition and substrate effects, the adsorption strength of the *OH intermediate is significantly weakened, and the potential-determining step of the ORR can even be altered. These findings establish a practical and effective framework for precisely adjusting intermediate binding energies through environmental control at electrochemical interfaces. The concept of substrate-engineered electric field modulation provides new opportunities for designing high-efficiency electrocatalytic devices.

4 Methods

4.1 Computational details

Spin-polarized DFT calculations were performed using the Vienna *ab initio* simulation package (VASP) [43, 44], with the VASPsol++ extension applied to account for solvation effects in electrochemical environments [45]. Ion–electron interactions were described using the projector augmented wave method [46], and the exchange-correlation energies were treated using the generalized gradient approximation of Perdew–Burke–Ernzerhof functional [47]. The energy cutoff for the plane wave basis expansion was set to 500 eV. Structural relaxations were carried out until the residual atomic forces on each atom were less than 0.02 eV·Å^{-1}. A Γ-centered 3 × 3 × 1 *k*-point mesh was used for structural relaxation, and a denser 5 × 5 × 1 mesh was used for electronic structure calculations. A vacuum spacing of 20 Å was introduced along the out-of-plane direction to avoid spurious interactions between periodic images. van der Waals interactions were included using the DFT-D3 method with Grimme's dispersion correction [48]. Solvent effects were modeled with a continuum dielectric of relative permittivity 78.4 to represent water [49]. For modeling the In_2S_3/FeN_4–C system, a 5 × 5 graphene supercell (the lattice constants $a = b = 12.34$ Å) was aligned with a 3 × 3 In_2Se_3 supercell ($a = b = 12.19$ Å), resulting in a lattice mismatch of only 1.24%. More detailed computational methods are described in the ESM.

Electronic Supplementary Material: Supplementary material (detailed description of computational methods about grand canonical simulation; thermodynamics of ORR on FeN_4–C based on constant charge method; effect of applied electric field on other ORR intermediates; charge density difference for the *OH-adsorbed FeN_4–C system; evaluation of stable configuration of FeN_4–C@In_2Se_3; and the plane-averaged electrostatic potential of In_2Se_3 substrate) is available in the online version of this article at https://doi.org/10.26599/NR.2026.94908460.

Data availability

All data needed to support the conclusions in the paper are presented in the manuscript and the Electronic Supplementary Material. Additional data related to this paper may be requested from the corresponding author upon request.

Acknowledgements

This work was supported by the National Key R&D Program of China (Nos. 2022YFA1203400 and 2021YFA1400100), the National Natural Science Foundation of China (Nos. 12274254, 22461160283, and 12204263), and the Local Innovative and Research Teams Project of Guangdong Pearl River Talents Program (No. 2017BT01N111).

Declaration of competing interest

All the contributing authors report no conflict of interests in this work.

Author contribution statement

Y. F. S.: Data curation, project administration, funding acquisition, validation, writing manuscript. Z. C. Z.: Project administration, validation, writing manuscript, formal analysis. J. L.: Conceptualization, supervision, project administration, funding acquisition, manuscript revision. All the authors have approved the final manuscript.

Use of AI statement

None.

References

[1] Tian, H.; Song, A. L.; Zhang, P.; Sun, K. A.; Wang, J. J.; Sun, B.;

Fan, Q. H.; Shao, G. J.; Chen, C.; Liu, H. et al. High durability of Fe–N–C single-atom catalysts with carbon vacancies toward the oxygen reduction reaction in alkaline media. *Adv. Mater.* **2023**, *35*, 2210714.

[2] Luo, J. M.; Zhang, Y. T.; Lu, Z.; Liu, C.; Xu, Y. S.; Chen, H.; Wang, Q.; Wu, D. X.; Dang, D.; Deng, Y. J. et al. Oxygen-coordinated Cr single-atom catalyst for oxygen reduction reaction in proton exchange membrane fuel cells. *Angew. Chem., Int. Ed.* **2025**, *64*, e202500500.

[3] Li, R. S.; Rao, P.; Wu, D. X.; Li, J.; Deng, P. L.; Miao, Z. P.; Tian, X. L. Understanding the bifunctional trends of Fe-based binary single-atom catalysts. *Adv. Sci.* **2023**, *10*, 2301566.

[4] Liu, J.; Zhu, J. Q.; Xu, H. X.; Cheng, D. J. Rational design of heteroatom-doped Fe–N–C single-atom catalysts for oxygen reduction reaction via simple descriptor. *ACS Catal.* **2024**, *14*, 6952–6964.

[5] Wang, Y. J.; Zhao, N. N.; Fang, B. Z.; Li, H.; Bi, X. T.; Wang, H. J. Carbon-supported Pt-based alloy electrocatalysts for the oxygen reduction reaction in polymer electrolyte membrane fuel cells: Particle size, shape, and composition manipulation and their impact to activity. *Chem. Rev.* **2015**, *115*, 3433–3467.

[6] Rebarchik, M.; Bhandari, S.; Kropp, T.; Mavrikakis, M. Insights into the oxygen evolution reaction on graphene-based single-atom catalysts from first-principles-Informed microkinetic modeling. *ACS Catal.* **2023**, *13*, 5225–5235.

[7] Zhong, L. X.; Li, S. Z. Unconventional oxygen reduction reaction mechanism and scaling relation on single-atom catalysts. *ACS Catal.* **2020**, *10*, 4313–4318.

[8] Liu, K.; Fu, J. W.; Lin, Y. Y.; Luo, T.; Ni, G. H.; Li, H. M.; Lin, Z.; Liu, M. Insights into the activity of single-atom Fe–N–C catalysts for oxygen reduction reaction. *Nat. Commun.* **2022**, *13*, 2075.

[9] Liu, T. Y.; Wang, Y.; Li, Y. F. How pH affects the oxygen reduction reactivity of Fe–N–C materials. *ACS Catal.* **2023**, *13*, 1717–1725.

[10] Jiang, F.; Li, Y. C.; Pan, Y. Design principles of single-atom catalysts for oxygen evolution reaction: From targeted structures to active sites. *Adv. Mater.* **2024**, *36*, 2306309.

[11] Liu, J. Q.; Chen, W. B.; Yuan, S.; Liu, T.; Wang, Q. High-coordination Fe–N_4SP single-atom catalysts via the multi-shell synergistic effect for the enhanced oxygen reduction reaction of rechargeable Zn–air battery cathodes. *Energy Environ. Sci.* **2024**, *17*, 249–259.

[12] Alvarado-Leal, L. A.; Paez-Ornelas, J. I.; Fernández-Escamilla, H. N.; Perez-Tijerina, E. G.; Guerrero-Sánchez, J.; Romo-Herrera, J. M.; Takeuchi, N. Influence of the atomic local environment on the ORR activity of single-atom catalysts in N-doped graphene. *ACS Appl. Energy Mater.* **2024**, *7*, 4794–4802.

[13] Zhang, P. X.; Liu, Y. Y.; Liu, S. L.; Zhou, L. M.; Wu, X. L.; Han, G. S.; Liu, T.; Sun, K.; Li, B. J.; Jiang, J. C. Precise design and modification engineering of single-atom catalytic materials for oxygen reduction. *Small* **2024**, *20*, 2305782.

[14] Song, W. Q.; Xiao, C. X.; Ding, J.; Huang, Z. C.; Yang, X. Y.; Zhang, T.; Mitlin, D.; Hu, W. B. Review of carbon support coordination environments for single metal atom electrocatalysts (SACS). *Adv. Mater.* **2024**, *36*, 2301477.

[15] Yang, X.; Xia, D. S.; Kang, Y. Q.; Du, H. D.; Kang, F. Y.; Gan, L.; Li, J. Unveiling the axial hydroxyl ligand on Fe–N_4–C electrocatalysts and its impact on the pH-dependent oxygen reduction activities and poisoning kinetics. *Adv. Sci.* **2020**, *7*, 2000176.

[16] Xia, D. S.; Tang, X.; Dai, S.; Ge, R. L.; Rykov, A.; Wang, J. H.; Huang, T. H.; Wang, K. W.; Wei, Y. P.; Zhang, K. et al. Ultrastable Fe–N–C fuel cell electrocatalysts by eliminating non-coordinating nitrogen and regulating coordination structures at high temperatures. *Adv. Mater.* **2023**, *35*, 2204474.

[17] Peng, L. S.; Yang, J.; Yang, Y. Q.; Qian, F. R.; Wang, Q.; Sun-Waterhouse, D.; Shang, L.; Zhang, T. R.; Waterhouse, G. I. N. Mesopore-rich Fe–N–C catalyst with FeN_4–O–NC single-atom sites delivers remarkable oxygen reduction reaction performance in alkaline media. *Adv. Mater.* **2022**, *34*, e2202544.

[18] Zhang, X.; Truong-Phuoc, L.; Asset, T.; Pronkin, S.; Pham-Huu, C. Are Fe–N–C electrocatalysts an alternative to Pt-based electrocatalysts for the next generation of proton exchange membrane fuel cells. *ACS Catal.* **2022**, *12*, 13853–13875.

[19] Hu, J. W.; Shang, W. Z.; Xin, C. C.; Guo, J. Y.; Cheng, X. S.; Zhang, S. L.; Song, S. C.; Liu, W.; Ju, F.; Hou, J. G. et al. Uncovering dynamic edge-sites in atomic Co–N–C electrocatalyst for selective hydrogen peroxide production. *Angew. Chem., Int. Ed.* **2023**, *62*, e202304754.

[20] Chu, Y. Y.; Luo, E. G.; Wei, Y.; Zhu, S. Y.; Wang, X.; Yang, L. T.; Gao, N. X.; Wang, Y.; Jiang, Z.; Liu, C. P. et al. Dual single-atom catalyst design to build robust oxygen reduction electrode via free radical scavenging. *Chem Catal.* **2023**, *3*, 100532.

[21] Zhou, S. L.; Chen, C.; Xia, J. W.; Li, L.; Qian, X. Y.; Yin, F. X.; He, G. Y.; Chen, Q.; Chen, H. Q. FeN_4S_1 single-atom sites anchored on three-dimensional porous carbon for highly efficient and durable oxygen electrocatalysis. *ACS Nano* **2024**, *18*, 32995–33004.

[22] Huang, S. Q.; Lin, F. M.; Wang, S. T.; Zeng, X. F.; Ling, H.; Hu, X. Y.; Shen, Z. G.; Cao, D. P. Asymmetric microenvironment tailoring strategies of atomically dispersed dual-site catalysts for oxygen reduction and CO_2 reduction reactions. *Adv. Mater.* **2024**, *36*, 2407974.

[23] Yan, W.; Chen, W. M.; Chen, Y. L. Recent design strategies for M–N–C single-atom catalysts in oxygen reduction: An entropy increase perspective. *Adv. Funct. Mater.* **2024**, *34*, 2401027.

[24] Wang, Y. Q.; Dan, X. H.; Wang, X.; Yi, Z. Y.; Fu, J. J.; Feng, Y. C.; Hu, J. S.; Wang, D.; Wan, L. J. Probing the synergistic effects of Mg^{2+} on CO_2 reduction reaction on CoPc by *in situ* electrochemical scanning tunneling microscopy. *J. Am. Chem. Soc.* **2022**, *144*, 20126–20133.

[25] Ji, S. G.; Kim, M. M.; Han, M. H.; Cho, J.; Son, Y.; Kim, Y. Y.; Jeong, J.; Kim, Z. H.; Chae, K. H.; Oh, H. S. et al. Alkali metal cations act as homogeneous cocatalysts for the oxygen reduction reaction in aqueous electrolytes. *Nat. Catal.* **2024**, *7*, 1330–1338.

[26] Cao, P. K.; Zhao, X. Y.; Liu, Y. M.; Zhang, H. G.; Zhao, K.; Chen, S.; Yu, H. T.; Dong, F.; Nichols, N. N.; Chen, J. G. et al. Highly efficient acidic electrosynthesis of hydrogen peroxide at industrial-level current densities promoted by alkali metal cations. *Angew. Chem., Int. Ed.* **2024**, *63*, e202406452.

[27] Lu, X. X.; Tu, W. G.; Zhou, Y.; Zou, Z. G. Effects of electrolyte ionic species on electrocatalytic reactions: Advances, challenges, and perspectives. *Adv. Energy Mater.* **2023**, *13*, 2300628.

[28] Vijay, S.; Gauthier, J. A.; Heenen, H. H.; Bukas, V. J.; Kristoffersen, H. H.; Chan, K. R. Dipole-field interactions determine the CO_2 reduction activity of 2D Fe–N–C single-atom catalysts. *ACS Catal.* **2020**, *10*, 7826–7835.

[29] Liu, M.; Pang, Y. J.; Zhang, B.; De Luna, P.; Voznyy, O.; Xu, J. X.; Zheng, X. L.; Dinh, C. T.; Fan, F. J.; Cao, C. H. et al. Enhanced electrocatalytic CO_2 reduction via field-induced reagent concentration. *Nature* **2016**, *537*, 382–386.

[30] Zi, X.; Zhou, Y. J.; Zhu, L.; Chen, Q.; Tan, Y.; Wang, X. Q.; Sayed, M.; Pensa, E.; Geioushy, R. A.; Liu, K. et al. Breaking K^+ concentration limit on Cu nanoneedles for acidic electrocatalytic CO_2 reduction to multi-carbon products. *Angew. Chem., Int. Ed.* **2023**, *62*, e202309351.

[31] Li, Z. W.; Zhou, X. J.; Liu, Y. Q.; Li, X. M.; Shen, Y.; Wen, M.; Lei, P. X.; Qian, L. H. Revealing the dynamic microenvironment of the Ag/CeO_2 surface for robust electrocatalytic CO_2 reduction. *ACS Catal.* **2025**, *15*, 15019–15032.

[32] Singh, M. R.; Kwon, Y.; Lum, Y.; Ager III, J. W.; Bell, A. T. Hydrolysis of electrolyte cations enhances the electrochemical reduction of CO_2 over Ag and Cu. *J. Am. Chem. Soc.* **2016**, *138*, 13006–13012.

[33] Wang, Q. L.; Hung, S. F.; Lao, K. J.; Huang, X.; Li, F. H.; Tao, H. B.;

Yang, H. B.; Liu, W.; Wang, W. J.; Cheng, Y. Q. et al. Breaking the linear scaling limit in multi-electron-transfer electrocatalysis through intermediate spillover. *Nat. Catal.* **2025**, *8*, 378–388.

[34] Chen, X.; Ma, H.; Wang, X.; Jin, H. Q.; Wu, Y.; Wang, S. B.; Xiao, Y. K.; Jiang, R.; Da, Y. M.; Fan, L. et al. Breaking the scaling relationship in water oxidation enabled by the electron buffering effect of the fullerene network. *J. Am. Chem. Soc.* **2025**, *147*, 20600–20611.

[35] Han, W.; Zheng, X. D.; Yang, K.; Tsang, C. S.; Zheng, F. Y.; Wong, L. W.; Lai, K. H.; Yang, T. F.; Wei, Q.; Li, M. J. et al. Phase-controllable large-area two-dimensional In_2Se_3 and ferroelectric heterophase junction. *Nat. Nanotechnol.* **2023**, *18*, 55–63.

[36] Ju, L.; Tan, X.; Mao, X.; Gu, Y. T.; Smith, S.; Du, A. J.; Chen, Z. F.; Chen, C. F.; Kou, L. Z. Controllable CO_2 electrocatalytic reduction via ferroelectric switching on single atom anchored In_2Se_3 monolayer. *Nat. Commun.* **2021**, *12*, 5128.

[37] Ju, L.; Shang, J.; Tang, X.; Kou, L. Z. Tunable photocatalytic water splitting by the ferroelectric switch in a 2D $AgBiP_2Se_6$ monolayer. *J. Am. Chem. Soc.* **2020**, *142*, 1492–1500.

[38] Ma, H.; Ye, X. Y.; Li, X. N.; Xu, Z. J.; Sun, Y. M. Ferroelectric polarization effects of single-atom catalysts on water oxidation. *Adv. Mater.* **2025**, *37*, 2500285.

[39] Wasileski, S. A.; Koper, M. T. M.; Weaver, M. J. Field-dependent electrode-chemisorbate bonding: Sensitivity of vibrational stark effect and binding energetics to nature of surface coordination. *J. Am. Chem. Soc.* **2002**, *124*, 2796–2805.

[40] Shetty, M.; Ardagh, M. A.; Pang, Y. T.; Abdelrahman, O. A.; Dauenhauer, P. J. Electric-field-assisted modulation of surface thermochemistry. *ACS Catal.* **2020**, *10*, 12867–12880.

[41] Jia, C. Y.; Wang, Q.; Yang, J.; Ye, K.; Li, X. Y.; Zhong, W. H.; Shen, H. J.; Sharman, E.; Luo, Y.; Jiang, J. Toward rational design of dual-metal-site catalysts: Catalytic descriptor exploration. *ACS Catal.* **2022**, *12*, 3420–3429.

[42] Jia, C. Y.; Li, B.; Yang, J.; Jiang, S.; Gu, Z. Y.; Sun, L.; Zhong, W. H.; Sharman, E.; Luo, Y.; Jiang, J. Prediction of C_2N-supported double-atom catalysts with individual/integrated descriptors for electrochemical and thermochemical CO_2 reduction. *J. Am. Chem. Soc.* **2025**, *147*, 16864–16875.

[43] Kresse, G.; Furthmüller, J. Efficiency of *ab initio* total energy calculations for metals and semiconductors using a plane-wave basis set. *Comput. Mater. Sci* **1996**, *6*, 15–50.

[44] Kresse, G.; Hafner, J. *Ab initio* molecular-dynamics simulation of the liquid-metal-amorphous-semiconductor transition in germanium. *Phys. Rev. B* **1994**, *49*, 14251–14269.

[45] Mathew, K.; Kolluru, V. S. C.; Mula, S.; Steinmann, S. N.; Hennig, R. G. Implicit self-consistent electrolyte model in plane-wave density-functional theory. *J. Chem. Phys.* **2019**, *151*, 234101.

[46] Kresse, G.; Joubert, D. From ultrasoft pseudopotentials to the projector augmented-wave method. *Phys. Rev. B* **1999**, *59*, 1758–1775.

[47] Perdew, J. P.; Burke, K.; Ernzerhof, M. Generalized gradient approximation made simple. *Phys. Rev. Lett.* **1996**, *77*, 3865–3868.

[48] Grimme, S.; Antony, J.; Ehrlich, S.; Krieg, H. A consistent and accurate *ab initio* parametrization of density functional dispersion correction (DFT-D) for the 94 elements H–Pu. *J. Chem. Phys.* **2010**, *132*, 154104.

[49] Mathew, K.; Sundararaman, R.; Letchworth-Weaver, K.; Arias, T. A.; Hennig, R. G. Implicit solvation model for density-functional study of nanocrystal surfaces and reaction pathways. *J. Chem. Phys.* **2014**, *140*, 084106.